

FIRST-YEAR *WILKINSON MICROWAVE ANISOTROPY PROBE (WMAP)*¹ OBSERVATIONS: TEMPERATURE-POLARIZATION CORRELATION

A. KOGUT,² D. N. SPERGEL,³ C. BARNES,⁴ C. L. BENNETT,² M. HALPERN,⁵ G. HINSHAW,² N. JAROSIK,⁴
M. LIMON,^{2,4,6} S. S. MEYER,⁷ L. PAGE,³ G. S. TUCKER,^{2,6,8} E. WOLLACK,² AND E. L. WRIGHT⁹

Received 2003 February 11; accepted 2003 May 20

ABSTRACT

The *Wilkinson Microwave Anisotropy Probe (WMAP)* has mapped the full sky in Stokes I , Q , and U parameters at frequencies of 23, 33, 41, 61, and 94 GHz. We detect correlations between the temperature and polarization maps significant at more than 10σ . The correlations are inconsistent with instrument noise and are significantly larger than the upper limits established for potential systematic errors. The correlations are present in all *WMAP* frequency bands with similar amplitude from 23 to 94 GHz and are consistent with a superposition of a cosmic microwave background (CMB) signal with a weak foreground. The fitted CMB component is robust against different data combinations and fitting techniques. On small angular scales ($\theta < 5^\circ$), the *WMAP* data show the temperature-polarization correlation expected from adiabatic perturbations in the temperature power spectrum. The data for $\ell > 20$ agree well with the signal predicted solely from the temperature power spectra, with no additional free parameters. We detect excess power on large angular scales ($\theta > 10^\circ$) compared to predictions based on the temperature power spectra alone. The excess power is well described by reionization at redshift $11 < z_r < 30$ at 95% confidence, depending on the ionization history. A model-independent fit to reionization optical depth yields results consistent with the best-fit Λ -dominated cold dark matter model, with best-fit value $\tau = 0.17 \pm 0.04$ at 68% confidence, including systematic and foreground uncertainties. This value is larger than expected given the detection of a Gunn-Peterson trough in the absorption spectra of distant quasars and implies that the universe has a complex ionization history: *WMAP* has detected the signal from an early epoch of reionization.

Subject headings: cosmic microwave background — cosmology: observations — instrumentation: polarimeters

1. INTRODUCTION

Linear polarization of the cosmic microwave background (CMB) results from anisotropic Thomson scattering of CMB photons by free electrons. By symmetry, an isotropic radiation field cannot generate a net polarization. Any net polarization results from the quadrupole moment of the CMB temperature distribution seen by each scatterer. Multiple scattering suppresses polarization by damping the temperature anisotropy; hence, CMB polarization originates primarily from epochs when the opacity was of the order of unity or less. Standard cosmological models predict two such epochs, corresponding to two characteristic angular scales. The first is the decoupling surface at redshift $z \approx 1089$, when the ionization fraction x_e abruptly falls from near unity to near zero. The acoustic horizon at

decoupling subtends an angle $\theta \approx 1^\circ$; polarization on these scales reflects conditions in the photon-baryon fluid just prior to recombination. Polarization data from decoupling complement measurements of the temperature anisotropy. Astrophysical sources generate additional polarization as ionizing radiation from the first collapsed objects reionizes the intergalactic medium. For reionization at redshift $z < 50$, the horizon is on large angular scales, $\theta > 5^\circ$. Polarization on these scales directly probes the poorly understood process of reionization.

Since CMB polarization originates at modest opacity, the underlying temperature anisotropy is not heavily damped and remains observable today. Precise predictions can be made of the average polarization pattern expected from a given power spectrum of temperature anisotropy (Rees 1968; Kaiser 1983; Bond & Efstathiou 1984; Coulson, Crittenden, & Turok 1994; Kamionkowski, Kosowsky, & Stebbins 1997; Zaldarriaga & Seljak 1997; Hu & White 1997; for recent reviews, see Kosowsky 1996; Hu & Dodelson 2002). The pattern of polarization on the sky is a vector field with both an amplitude and direction at each point and can be separated into two scalar fields, one giving the curl and the other the gradient component (called B - and E -modes in analogy with electromagnetic fields). The Degree Angular Scale Interferometer (DASI) collaboration has detected CMB polarization on angular scales $\sim 0.5^\circ$ (Kovac et al. 2002). DASI reports an E -mode signal significant at 4.9σ and a temperature-polarization (TE) correlation significant at 2σ . Both signals are consistent with the “concordance” cosmological model (spatially flat model dominated by a cosmological constant and cold dark

¹ *WMAP* is the result of a partnership between Princeton University and the NASA Goddard Space Flight Center. Scientific guidance is provided by the *WMAP* Science Team.

² NASA Goddard Space Flight Center, Code 685, Greenbelt, MD 20771; alan.j.kogut@nasa.gov.

³ Department of Astrophysical Sciences, Princeton University, Princeton, NJ 08544.

⁴ Department of Physics, Jadwin Hall, Princeton, NJ 08544.

⁵ Department of Physics and Astronomy, University of British Columbia, Vancouver, BC V6T 1Z1, Canada.

⁶ National Research Council Fellow.

⁷ Departments of Astrophysics and Physics, EFI, and CfCP, University of Chicago, Chicago, IL 60637.

⁸ Department of Physics, Brown University, Providence, RI 02912.

⁹ Department of Astronomy, UCLA, P.O. Box 951562, Los Angeles, CA 90095-1562.

matter; see, e.g., Hu & Dodelson 2002) and support an adiabatic origin for the CMB temperature anisotropy.

WMAP has mapped the full sky in the Stokes I , Q , and U parameters on angular scales $\theta > 0.2^\circ$ in five frequency bands centered at 23, 33, 41, 61, and 94 GHz (Bennett et al. 2003a). *WMAP* was not designed solely as a polarimeter, in the sense that none of its detectors are sensitive only to polarization. Incident radiation in each differencing assembly (DA) is split by an orthomode transducer (OMT) into two orthogonal linear polarizations (Page et al. 2003a; Jarosik et al. 2003). Each OMT is oriented so that the electric field directions accepted in the output rectangular waveguides lie at $\pm 45^\circ$ with respect to the y - z symmetry plane of the satellite (see Bennett et al. 2003a, Fig. 2 for the definition of the satellite coordinate system). The two orthogonal polarizations from the OMT are measured by two independent radiometers. Each radiometer differences the signal in the accepted polarization between two positions on the sky (the A and B beams), separated by $\sim 140^\circ$.

The signal from the sky in each direction \mathbf{n} can be decomposed into the Stokes parameters:

$$T(\mathbf{n}) = I(\mathbf{n}) + Q(\mathbf{n}) \cos 2\gamma + U(\mathbf{n}) \sin 2\gamma, \quad (1)$$

where we define the angle γ from a meridian through the Galactic poles to the projection on the sky of the E -plane of each output port of the OMT (Fig. 1). In principle, by tracking the orientation of the OMTs on the sky as the satellite scan pattern observes each sky pixel in different orientations, each radiometer could independently produce a map of the Stokes I , Q , and U parameters. In practice, the non-uniform coverage of γ at each pixel would generate significant correlations between the fitted Stokes parameters, allowing leakage of the dominant temperature anisotropy into the much fainter polarization maps. We avoid this problem by differencing the outputs of the two radiometers in each DA in the time-ordered data. Denoting the two radiometers by subscripts 1 and 2, the instantaneous outputs are

$$\begin{aligned} \Delta T_1 &= I(\mathbf{n}_A) + Q(\mathbf{n}_A) \cos 2\gamma_A + U(\mathbf{n}_A) \sin 2\gamma_A \\ &\quad - I(\mathbf{n}_B) - Q(\mathbf{n}_B) \cos 2\gamma_B - U(\mathbf{n}_B) \sin 2\gamma_B, \end{aligned}$$

$$\begin{aligned} \Delta T_2 &= I(\mathbf{n}_A) - Q(\mathbf{n}_A) \cos 2\gamma_A - U(\mathbf{n}_A) \sin 2\gamma_A \\ &\quad - I(\mathbf{n}_B) + Q(\mathbf{n}_B) \cos 2\gamma_B + U(\mathbf{n}_B) \sin 2\gamma_B. \end{aligned} \quad (2)$$

The sum,

$$\Delta T_I \equiv \frac{1}{2}(\Delta T_1 + \Delta T_2) = I(\mathbf{n}_A) - I(\mathbf{n}_B), \quad (3)$$

is thus proportional to the unpolarized intensity, while the difference,

$$\begin{aligned} \Delta T_P &\equiv \frac{1}{2}(\Delta T_1 - \Delta T_2) \\ &= Q(\mathbf{n}_A) \cos 2\gamma_A + U(\mathbf{n}_A) \sin 2\gamma_A \\ &\quad - Q(\mathbf{n}_B) \cos 2\gamma_B - U(\mathbf{n}_B) \sin 2\gamma_B, \end{aligned} \quad (4)$$

is proportional only to the polarization. We produce full-sky maps of the Stokes I , Q , and U parameters from the sum and difference time-ordered data using an iterative mapping algorithm. Since the polarization is faint, the Q and U maps are dominated by instrument noise and converge rapidly (Hinshaw et al. 2003a).

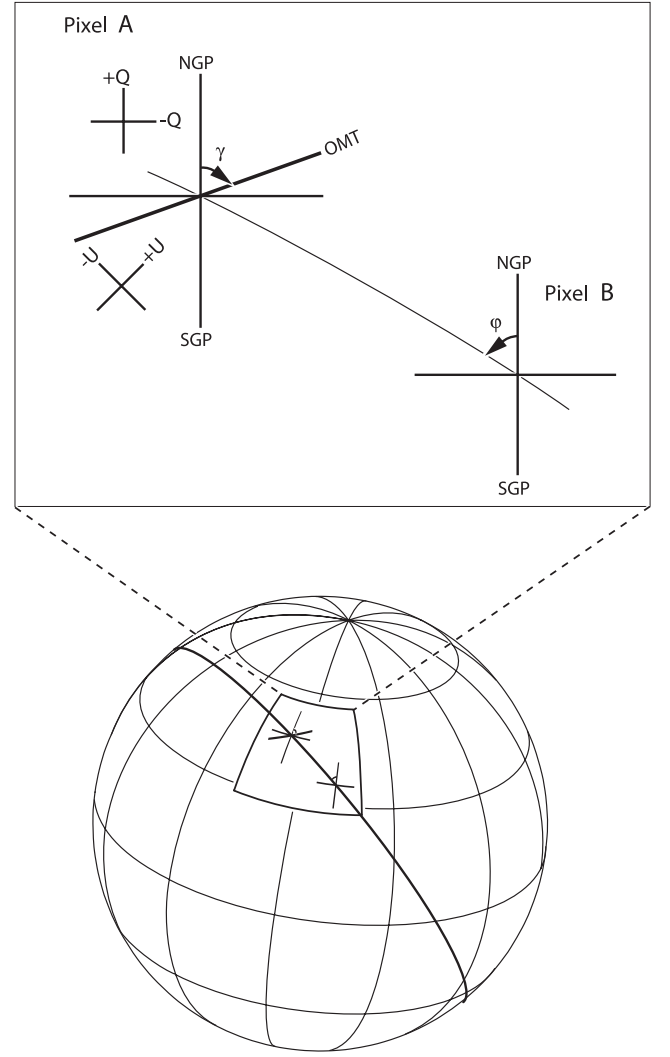


FIG. 1.—Geometry for Stokes Q and U parameters. *WMAP* measures polarization by differencing two orthogonal polarization channels, then solving for Q and U as the spacecraft compound spin projects the OMT onto the sky at different angles γ relative to the Galactic meridians. All analysis uses coordinate-independent quantities Q' and U' defined with respect to the great circle connecting a pair of pixels (see text).

The Stokes Q and U components depend on a specific choice of coordinate system. For each pair of pixels, we define coordinate-independent quantities

$$\begin{aligned} Q' &= Q \cos(2\phi) + U \sin(2\phi), \\ U' &= U \cos(2\phi) - Q \sin(2\phi), \end{aligned} \quad (5)$$

where the angle ϕ rotates the coordinate system about the outward-directed normal vector to put the meridian along the great circle connecting the two positions on the sky (Kamionkowski et al. 1997; Zaldarriaga & Seljak 1997). All of our analyses use these coordinate-independent linear combinations of the Q and U sky maps.

Simulations of the mapping algorithm demonstrate that *WMAP* can accurately recover the polarization pattern on the sky, even after allowing for residual calibration uncertainty in the individual radiometer channels. However, non-ideal instrumental signals affect the Q and U sky maps to a greater extent than the unpolarized I maps. The spacecraft

spin about its z -axis sweeps the beams across the sky in a direction 45° from the OMT orientation, preferentially coupling signals not fixed on the sky into the U map. Residual striping exists to a lesser extent in the I and Q maps. Systematic errors in the individual Q and U maps are not yet fully assessed; consequently, we defer detailed analysis of the Q and U maps to a later paper. Cross-correlations between maps are largely unaffected by striping or any other channel-specific signal, allowing much simpler analysis of the faint polarization signal than would be possible for the individual Q or U maps. This paper discusses the TE correlation in the *WMAP* first-year sky maps.

We compute the temperature-polarization cross-correlation using three different techniques: the two-point correlation function, a quadratic estimator for the power spectrum, and a “template” comparison in pixel space between the polarization maps and the predicted polarization given the observed pattern of temperature anisotropy. All three methods yield similar results despite disparate treatments of the data.

2. CORRELATION FUNCTION

The simplest measure of temperature-polarization cross-correlation is the two-point angular correlation function,

$$C^{IQ}(\theta) = \frac{\sum_{ij} I_i Q_j w_i w_j}{\sum_{ij} w_i w_j}, \quad (6)$$

where i and j are pixel indices and w are the weights. To avoid possible effects of $1/f$ noise, we force the temperature map to come from a different frequency band than the polarization maps and thus use the temperature map at 61 GHz (V band) for all correlations except the V-band polarization maps, which we correlate against the 41 GHz (Q band) temperature map. Since *WMAP* has a high signal-to-noise ratio measurement of the CMB temperature anisotropy, we use unit weight ($w_i = 1$) for the temperature maps and noise weight ($w_j = N_j/\sigma_0^2$) for the polarization maps, where N_j is the effective number of observations in each pixel j and σ_0 is the standard deviation of the white noise in the time-ordered data (Table 1 of Bennett et al. 2003b). We compare the correlation functions with Monte Carlo simulations of a null model, which simulates the temperature anisotropy using the best-fit Λ -dominated cold dark matter (Λ CDM) model (Spergel et al. 2003) but forces the polarization signal to zero. Each realization generates a CMB sky in Stokes I , Q , and U parameters, convolves this simulated sky with the beam pattern for each DA, and then adds uncorrelated instrument noise to each pixel in each map. We then co-add the simulated skies in each frequency band and compute $C^{IQ}(\theta)$ using the same software for both the *WMAP* data and the simulations. All analysis uses only pixels outside the *WMAP* Kp0 foreground emission mask (Bennett et al. 2003c), approximately 76% of the full sky.

Figure 2 shows $C^{IQ}(\theta)$ derived by co-adding the individual correlation functions for the frequencies 41, 61, and 94 GHz (Q, V, and W bands), which are least likely to be affected by Galactic foregrounds. The gray band shows the 68% confidence interval for the null simulations. It is clear that *WMAP* detects a temperature-polarization signal at high statistical confidence and that signals exist on both large and small angular scales. We define a goodness-of-fit

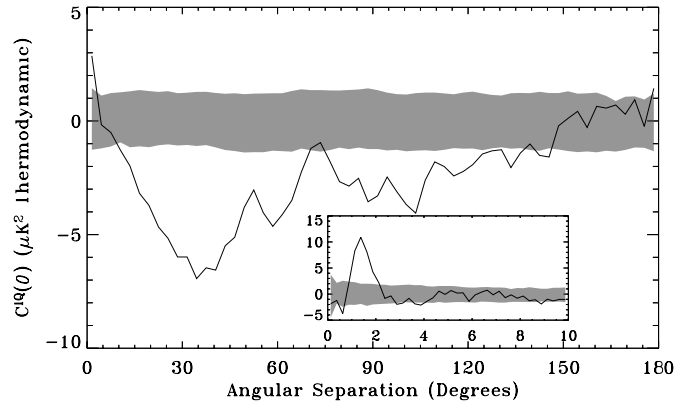


FIG. 2.—Temperature-polarization correlation function for *WMAP* co-added QVW data. The gray band shows the 68% confidence interval for similar co-added data taken from Monte Carlo simulations without polarization. The inset shows data for $\theta < 10^\circ$. The data are inconsistent with no temperature-polarization cross-correlations at more than 10σ . Note that the data are not independent between angular bins.

statistic

$$\chi^2 = \sum_{ab} (C_{WMAP}^{IQ} - \langle C_{sim}^{IQ} \rangle)_a \mathbf{M}_{ab}^{-1} (C_{WMAP}^{IQ} - \langle C_{sim}^{IQ} \rangle)_b, \quad (7)$$

where C_{WMAP}^{IQ} is the co-added correlation function from *WMAP* data, $\langle C_{sim}^{IQ} \rangle$ is the mean from the Monte Carlo simulations, and \mathbf{M} is the covariance matrix between angular bins a and b derived from the simulations. We find $\chi^2 = 207$ for 78 degrees of freedom when comparing *WMAP* to the null model: *WMAP* detects temperature-polarization correlations significant at more than 10σ .

2.1. Systematic Error Analysis

Having detected a significant signal in the data, we must determine whether this signal has a cosmological origin or results from systematic errors or foreground sources. We test the convergence of the mapping algorithm using end-to-end simulations, comparing maps derived from simulated time-ordered data with the input maps used to generate the simulated time series. The simulations include all major instrumental effects, including beam ellipticity, radiometer performance, and instrument noise (including the $1/f$ component), and are processed using the same map-making software as the *WMAP* data (Hinshaw et al. 2003a). The Q and U maps converge rapidly, within the 30 iterations required to derive the calibration solution. Correlations in the time-ordered data introduce an anticorrelation in the U map at angles corresponding to the beam separation, with an amplitude 0.5% of the noise in the map. This effect is independent for each radiometer and does not affect temperature-polarization cross-correlations. Similarly, residual $1/f$ noise in the time series can create faint striping in the maps but does not affect cross-correlations.

The largest potential systematic error in the temperature-polarization cross-correlation results from bandpass mismatches in the amplification/detection chains. We calibrate the *WMAP* data in thermodynamic temperature using the Doppler dipole from the satellite’s orbit about the Sun as a beam-filling calibration source (Hinshaw et al. 2003a). Astrophysical sources with a spectrum other than a 2.7 K blackbody are thus slightly miscalibrated. The amplitude is

dependent on the product of the source spectrum with the unique bandpass of each radiometer. If the bandpasses in each radiometer were identical, the effect would cancel for any frequency spectrum, but differences in the bandpasses between the two radiometers in each DA generate a nonzero residual in the difference signal used to generate polarization maps (eq. [4]). This signal is spatially correlated with the unpolarized foreground intensity but is independent of the orientation of the radiometers on the sky (polarization angle γ). In the limit of uniform sampling of γ , this term drops out of the sky-map solution. However, the *WMAP* scan pattern does not view each pixel in all orientations; unpolarized emission with a non-CMB spectrum can thus be aliased into polarization if the bandpasses of the two radiometers in each DA are not identical. This is a significant problem only at 23 GHz (K band), at which the foregrounds are brightest and the bandpass mismatch is largest.

We quantify the effect of bandpass mismatch using end-to-end simulations. For each time-ordered sample, we compute the signal in each radiometer using an unpolarized foreground model and the measured passbands in each output channel (Jarosik et al. 2003). We then generate maps from the simulated data using the *WMAP* first-year sky coverage and compute $C^{IQ}(\theta)$ using the output I , Q , and U maps from the simulation. Figure 3 shows the predicted signal at the K band. We treat this as an angular template and compute the least-squares fit of the *WMAP* data to this bandpass template to determine the amplitude of the effect in the observed correlation functions. We correct the *WMAP* correlation functions $C^{IQ}(\theta)$ and $C^{IU}(\theta)$ at the K and Ka bands by subtracting the best-fit template amplitudes. The fitted signal has a peak amplitude of $8 \mu\text{K}^2$ at 23 GHz and $5 \mu\text{K}^2$ at 33 GHz. No other channel has a statistically significant detection of this effect.

Sidelobe pickup of polarized emission from the Galactic plane can also produce spurious polarization at high latitudes in the Q and U maps. We estimate this effect using the measured far sidelobe response for each beam in each polarization (Barnes et al. 2003). The simplest approach would be to estimate the signal in each time-ordered sample, convolving the full-sky sidelobe response with the Stokes I , Q , and U maps given the instantaneous orientation of the beams for each sample. Such an approach is computationally expensive. We instead approximate the signal in each pixel by convolving the full-sky sidelobe response with the first-year Q and U maps. For each pixel, we fix one beam on that pixel while sweeping the other beam through all orientations achieved in flight. The average from the convolution yields the sidelobe contribution for the pixel in question. Details of the sidelobe maps are presented in Barnes et al. (2003). We correlate the sidelobe maps with the temperature anisotropy maps in each channel to estimate the systematic error in the temperature-polarization correlation. Sidelobe pickup of polarized structure in the Galactic plane is less than $1 \mu\text{K}^2$ in $C^{IQ}(\theta)$ at 23 GHz and below $0.1 \mu\text{K}^2$ in all other bands. The effect of bandpass mismatch in the far sidelobes (as opposed to the main beam) is similarly weak, with limits of $1.3 \mu\text{K}^2$ at 23 GHz and less than $0.05 \mu\text{K}^2$ in all other bands. We correct the polarization maps for the estimated sidelobe signal and propagate the associated systematic uncertainty throughout our analysis. Note that all of these systematic errors depend on the Galactic foregrounds and have different frequency dependence than CMB polarization.

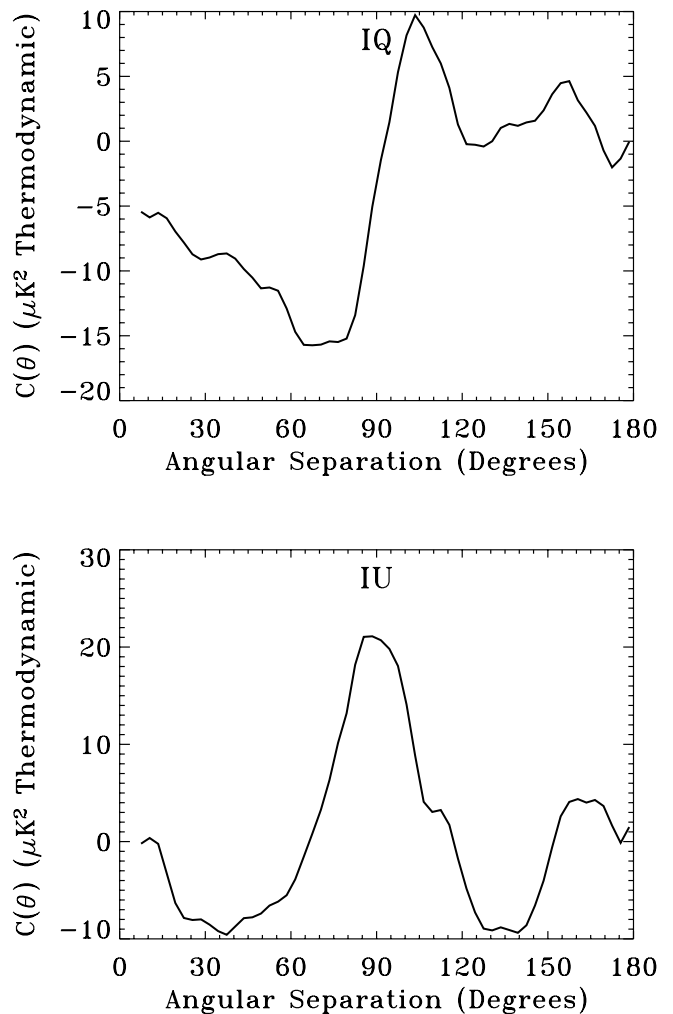


FIG. 3.—Angular templates for potential systematic errors caused by bandpass mismatch between the two radiometers in each DA. We fit this template to the correlation functions from each DA to detect or limit systematic errors related to bandpass mismatch in the main beam. The effect is significant only in the K and Ka bands, which have the brightest unpolarized foregrounds.

Other instrumental effects are negligible. We measure polarization by differencing the outputs of the two radiometers in each DA (eq. [4]). Calibration errors (as opposed to the bandpass effect discussed above) can alias temperature anisotropy into a spurious polarization signal. We have simulated the uncertainty in the calibration solution using both realistic gain drifts and drifts 10 times larger than observed in flight (Hinshaw et al. 2003a). Gain drifts (either intrinsic or thermally induced) contribute less than $1 \mu\text{K}^2$ to $C^{IQ}(\theta)$ in the worst band.

Null tests provide an additional check for systematic errors. Thomson scattering of scalar temperature anisotropy produces a curl-free polarization pattern. A nonzero cosmological signal is thus expected only for the IQ (TE) correlation, whereas systematic errors or foreground sources can affect both the IQ and IU (temperature/B-mode polarization [TB]) correlations. We also test linear combinations of radiometer maps that cancel the polarization signal but that test for systematic effects. We compute the IQ and IU correlation functions by correlating the Stokes I sum map from the Q or V band (as noted above) with the

TABLE 1
NULL TESTS FOR IQ AND IU SUM AND DIFFERENCE DATA^a

CORRELATION	RANGE	DEGREES OF FREEDOM	SUM MAP ^b		DIFFERENCE MAP ^c	
			χ^2	Probability ^d	χ^2	Probability ^d
IQ	$\theta < 5^\circ$	20	62.1	3×10^{-6}	23.6	0.26
IQ	$\theta \geq 5^\circ$	58	145.1	2×10^{-9}	66.0	0.22
IU	$\theta < 5^\circ$	20	30.9	0.06	10.8	0.95
IU	$\theta \geq 5^\circ$	58	66.1	0.22	50.4	0.95

^a A χ^2 comparison of the *WMAP* correlation functions $C^{IQ}(\theta)$ and $C^{IU}(\theta)$ with a null hypothesis of CMB temperature anisotropy and instrument noise but no polarization. Temperature-polarization signals of cosmic origin should contribute only to $C^{IQ}(\theta)$ in the sum maps. All other tests are consistent with the null hypothesis.

^b Polarization sum maps $(Q1 + Q2)/2$, $(V1 + V2)/2$, $(W1 + W2)/2$, and $(W3 + W4)/2$ co-added with noise weights.

^c Polarization difference maps $(Q1 - Q2)/2$, $(V1 - V2)/2$, $(W1 - W2)/2$, and $(W3 - W4)/2$ co-added with noise weights.

^d Probability to randomly obtain χ^2 larger than the measured value.

polarization *difference* maps $(Q1 - Q2)/2$, $(V1 - V2)/2$, $(W1 - W2)/2$, and $(W3 - W4)/2$. We then co-add the results with their noise weights and compare the co-added result for the polarization difference maps with a similar computation for the polarization sum maps. The temperature (Stokes I) map in all cases is a sum map; the test is thus primarily sensitive to systematic errors in the polarization data.

Table 1 shows results of the null tests. We compare $C^{IQ}(\theta)$ and $C^{IU}(\theta)$ for the sum and difference maps with a null hypothesis that the data consist of Stokes I and instrument noise, with no polarization in the Stokes Q or U maps. We break the data into two angular regimes to differentiate between signals at decoupling versus reionization. We find a clear signal detection for $C^{IQ}(\theta)$ in the sum map for both angular scales. All other tests are consistent with instrument noise; there is no evidence for additional systematic errors in the temperature-polarization cross-correlation.

2.2. Foregrounds

Galactic emission is not a strong contaminant for CMB temperature anisotropy but could be significant in polarization. *WMAP* measurements of unpolarized foreground emission show synchrotron, free-free, and thermal dust emission all sharing significant spatial structure (Bennett et al. 2003c). Of these components, only synchrotron emission is expected to generate significant polarization; other sources such as spinning dust are limited to less than 5% of the total intensity at 33 GHz.

Synchrotron emission from electrons accelerated in the Galactic magnetic field is the dominant unpolarized foreground at frequencies below ~ 50 GHz. Although it is known to be linearly polarized, previous radio surveys provide little guidance for the high-latitude polarization at millimeter wavelengths. Extrapolation of radio polarization maps (Brouw & Spoelstra 1976) to millimeter wavelengths indicates a polarization fraction between 10% and 50% depending on Galactic latitude (Lubin & Smoot 1981). The unpolarized component has angular power spectrum $c_\ell \propto \ell^{-2}$, while the CMB power spectrum rises to a set of peaks on angular scales $\theta \approx 1^\circ$ (e.g., Fig. 10b of Bennett et al. 2003c). The angular dependence of the *polarized* foreground component is expected to be even steeper (Baccigalupi et al. 2001; Bruscoli et al. 2002; Tucci et al. 2002), suggesting that foreground polarization is most likely

to affect temperature-polarization correlations on large angular scales. Radio maps at low Galactic latitude, however, demonstrate that the polarization intensity is not necessarily well correlated with the unpolarized intensity, complicating template analysis for temperature-polarization cross-correlations (Uyaniker et al. 1998, 1999). We thus use the frequency dependence of the measured temperature-polarization cross-correlation to separate cosmic from foreground signals.

Foreground polarization above 40 GHz is faint; fitting the correlation functions at 41, 61, and 94 GHz (Q, V, and W bands) to a single power law $C^{IQ}(\theta, \nu) = C_0^{IQ}(\theta)(\nu/\nu_0)^\beta$ yields spectral index $\beta = -0.4 \pm 0.4$, consistent with a CMB signal ($\beta = 0$) and inconsistent with the spectral indexes expected for synchrotron ($\beta \approx -3$), spinning dust ($\beta \approx -2$), or thermal dust ($\beta \approx 2$). The measured signal cannot be produced solely by a single foreground emission component (unless the fractional polarization of the foreground emission has a compensating frequency dependence, which seems unlikely).

A two-component fit,

$$C^{IQ}(\theta, \nu) = C_{\text{CMB}}^{IQ}(\theta) + C_{\text{Gal}}^{IQ}(\theta) \left(\frac{\nu}{\nu_0} \right)^\beta, \quad (8)$$

tests for the superposition of a CMB component with a single foreground component. Figure 4 shows the resulting decomposition into CMB and foreground components. We obtain a marginal detection of a foreground component with best-fit spectral index $\beta = -3.7 \pm 0.8$, consistent with synchrotron emission. We test for consistency or possible residual systematic errors by repeating the fit using different temperature maps and different combinations of *WMAP* polarization channels. The fitted CMB component (Fig. 4, *left*) is robust against all combinations of frequency channels and fitting techniques. Note the agreement in Figure 4 between nearly independent data sets: the co-added QVW data (uncorrected for foreground emission) and the KKaQ data (corrected for foreground emission). We obtain additional confirmation by replacing the V-band temperature map in the cross-correlation (eq. [6]) with the ‘‘internal linear combination’’ temperature map designed to suppress foreground emission (Bennett et al. 2003c). The fitted CMB component does not change. We test for systematic errors by replacing the temperature map with the *COBE*

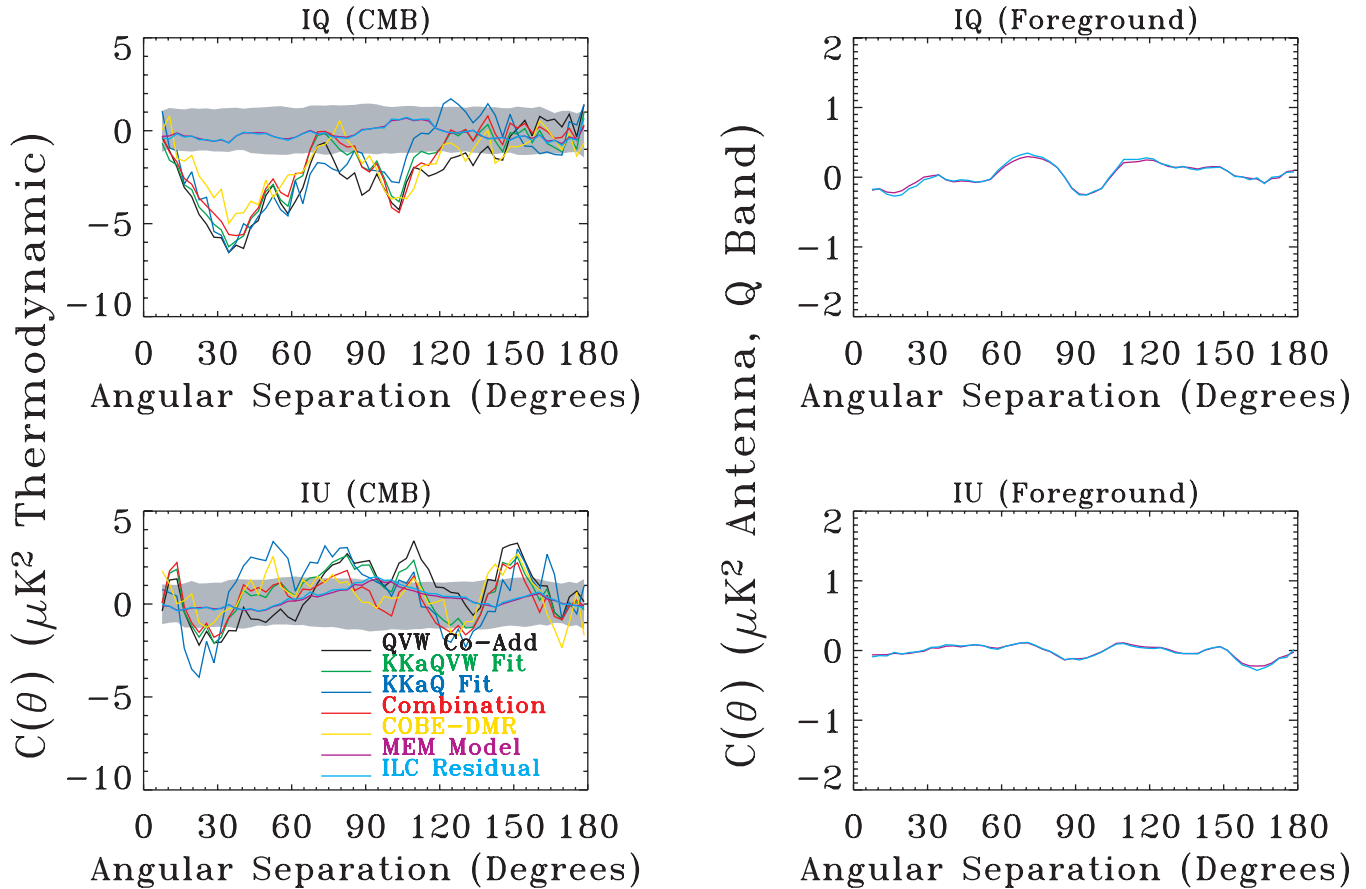


FIG. 4.—Fitted CMB (*left*) and foreground (*right*) components from a multifrequency decomposition of the measured two-point correlation functions. *Top*: IQ (TE) correlation. *Bottom*: IU (TB) correlation. The CMB component is shown in units of thermodynamic temperature, while the foreground is shown in antenna temperature evaluated at 41 GHz. Different colors show the effect of using different temperature maps in the cross-correlation or including different polarization frequency channels in the CMB-foreground decomposition. “Co-add” refers to a noise-weighted linear combination of the correlation functions computed for individual frequency channels. “Fit” refers to a two-component fit (eq. [8]) using the specified polarization frequency channels. The gray band shows the 68% confidence interval for the CMB component for the KKaQVW fit (which has the smallest statistical uncertainty) assuming CMB temperature anisotropy and instrument noise but no CMB polarization. “Combination” and “COBE DMR” replace the temperature map in eq. (6) with maps with reduced foreground emission: either the *WMAP* internal linear combination map or the *COBE* DMR map of the CMB temperature. “MEM Model” and “ILC Residual” replace the temperature map in eq. (6) with maps dominated by foreground emission: either the *WMAP* maximum-entropy foreground model or the residual map produced by subtracting the internal linear combination map from the individual temperature maps at each frequency. The fitted CMB component is stable as different frequency channels and data sets are analyzed. Foreground emission is faint compared to the cosmic signal.

Differential Microwave Radiometer (DMR) map of the CMB temperature (Bennett et al. 1996), excluding *any* instrumental correlation between the temperature and polarization data. Again, the results are unchanged.

We further constrain foreground contributions by computing the cross-correlation between the *WMAP* polarization data and temperature maps dominated by foregrounds. We replace the temperature map in equation (6) with either the *WMAP* maximum-entropy foreground model (Bennett et al. 2003c) or a “residual” foreground map created by subtracting the internal linear combination CMB map from the individual *WMAP* temperature maps. We then correlate the foreground temperature map against the *WMAP* polarization data in each frequency band and fit the resulting correlation functions to CMB and foreground components (eq. [8]). The two foreground maps provide nearly identical results. The fitted CMB component has nearly zero amplitude, consistent with the instrument noise. The fitted foreground has amplitude $0.5 \pm 0.1 \mu\text{K}^2$ at $\nu_0 = 41$ GHz, with best-fit index $\beta = -3.4$, consistent with synchrotron emission.

3. POLARIZATION CROSS-POWER SPECTRA

In a second analysis method, we compute the angular power spectrum of the temperature-polarization correlations using a quadratic estimator (Appendix A). The power spectrum is the Legendre transform of the two-point correlation function and is more commonly encountered for theoretical predictions. We compute c_ℓ^{TE} and c_ℓ^{TB} individually for each *WMAP* frequency band, using uniform weight for the temperature map and noise weight for the polarization maps. We then combine the angular power spectra, using noise-weighted QVW data for $\ell > 21$, for which foregrounds are insignificant, and a fit to CMB plus foregrounds using all five frequency bands for $\ell \leq 21$. Since foreground contamination is weak, we gain additional sensitivity in this analysis by using the Kp2 sky cut, retaining 85% of the sky.

We estimate the uncertainty in each ℓ -bin using the covariance matrix \mathbf{M} for the polarization cross-power spectrum. Based on our analysis of the c_ℓ^{TT} covariance matrix (Hinshaw et al. 2003b), the c_ℓ^{TE} covariance matrix has the

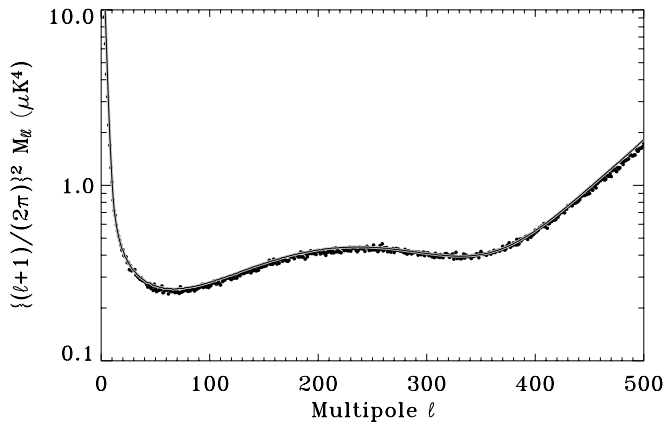


FIG. 5.—Diagonal elements of the covariance matrix for the c_ℓ^{TE} polarization cross-power spectrum. Points show the diagonal elements computed from 7500 Monte Carlo simulations. The solid line shows the analytical model (eq. [10]). Note we multiply $M_{\ell\ell}$ by $[(\ell+1)/2\pi]^2$ to match the units in Figs. 7 and 8.

form along the diagonal of

$$\mathbf{M}_{\ell\ell} = \langle c_\ell^{\text{TE}} c_\ell^{\text{TE}} \rangle - \langle c_\ell^{\text{TE}} \rangle^2 \quad (9)$$

$$\simeq \frac{(c_\ell^{\text{TT}} + n_{\text{TT}}/w_\ell)(c_\ell^{\text{EE}} + n_{\text{EE}}/w_\ell) + (c_\ell^{\text{TE}})^2}{(2\ell+1)f_{\text{sky}}f_{\text{sky}}^{\text{eff}}}, \quad (10)$$

where n_{TT} and n_{EE} are the TT and EE noise bias terms, w_ℓ is the effective window function for the combined maps (Page et al. 2003b), c_ℓ^{TT} and c_ℓ^{EE} are the temperature and polarization angular power spectra, $f_{\text{sky}} = 0.85$ is the fractional sky coverage for the Kp2 mask, and $f_{\text{sky}}^{\text{eff}} = f_{\text{sky}}/1.14$ for noise weighting. We take the c_ℓ^{TT} term from the measured temperature power spectra (Hinshaw et al. 2003b) and the c_ℓ^{EE} term predicted by the best-fit Λ CDM model (Spergel et al. 2003) (allowing c_ℓ^{EE} to vary as a function of optical depth in the likelihood analysis). Figure 5 compares the analytic expression for the diagonal elements of the covariance matrix with the mean derived from 7500 Monte Carlo simulations. The analytic form (eq. [10]) accurately describes the simulations. We approximate the off-diagonal terms using the geometric mean of the covariance matrix terms for uniform and noise weighting (Hinshaw et al. 2003b),¹⁰

$$\mathbf{M}_{\ell\ell'} \simeq (\mathbf{M}_{\ell\ell}\mathbf{M}_{\ell'\ell'})^{0.5} r_{\Delta\ell}. \quad (11)$$

Figure 6 shows the off-diagonal terms $r_{\Delta\ell}$ measured from Monte Carlo simulations. The largest contribution, -2.8% , is at $\Delta\ell = 2$ from the symmetry of our sky cut and noise coverage. The total anticorrelation is $\sum_{\Delta\ell \neq 0} r_{\Delta\ell} = -0.124$. Because of this anticorrelation, the error bars for the binned c_ℓ^{TE} are slightly smaller than the naive estimate. A second method of estimating the errors relies on end-to-end simulations derived from simulated time-ordered data consisting solely of instrument noise (including the estimated contribution from $1/f$ fluctuations). We have generated 11 “noise” sky maps each in Stokes I , Q , and U and computed the variance in TE directly from the variance in the simulated signal. These two approaches yield errors that are consistent

¹⁰ Note that Hinshaw et al. (2003b) define off-diagonal elements in terms of the inverse covariance matrix, which differs from $r_{\Delta\ell}$ by a sign.

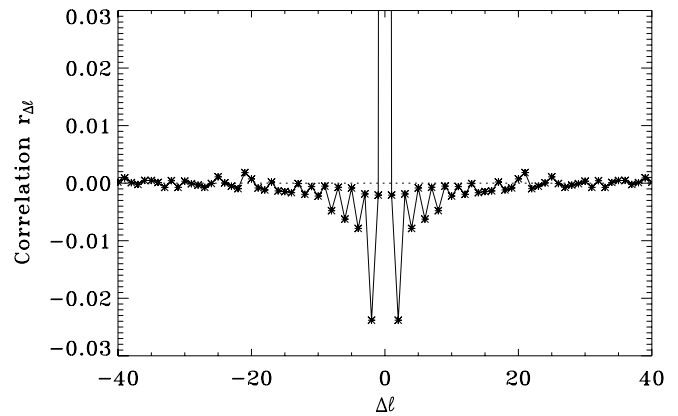


FIG. 6.—Off-diagonal correlations $r_{\Delta\ell}$ in the covariance matrix for the c_ℓ^{TE} polarization cross-power spectrum, computed from simulations. All values are normalized to $r_{\Delta\ell} = 1$ at $\Delta\ell = 0$. The dotted line shows $r_{\Delta\ell} = 0$ for comparison. The anticorrelation at $\Delta\ell = 2$ results from the spatial symmetry of the sky cut and noise coverage.

to better than 5%. Since there are $2\ell+1$ multipoles at each ℓ -value, the fractional uncertainty expected in the Monte Carlo variance is $\{2/[11(2\ell+1)f_{\text{sky}}]\}^{0.5}$, in agreement with this result.

Figure 7 shows the polarization cross-power spectra for the WMAP first-year data. The solid line shows the predicted signal for adiabatic CMB perturbations, based only on a fit to the measured temperature angular power spectrum c_ℓ^{TT} (Spergel et al. 2003; Hinshaw et al. 2003b). Two features are apparent. The TE data on degree angular scales ($\ell > 20$) are in excellent agreement with a priori predictions of adiabatic models (Coulson et al. 1994). Other than the specification of adiabatic perturbations, there are no free parameters; the solid line is not a fit to c_ℓ^{TE} . The χ^2 of 24.2 for 23 degrees of freedom indicates that the CMB anisotropy is dominated by adiabatic perturbations. On large

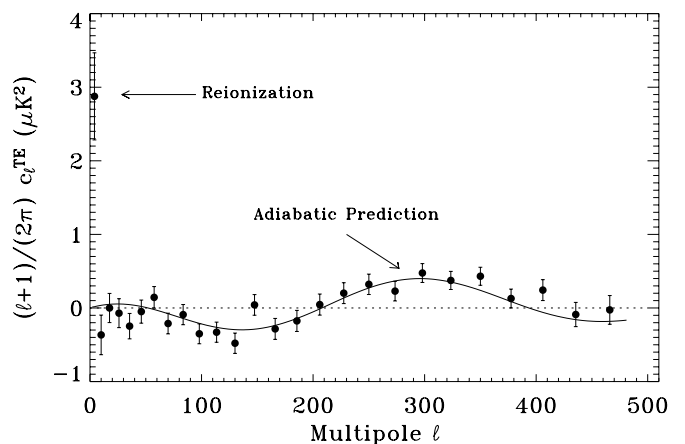


FIG. 7.—Polarization cross-power spectra c_ℓ^{TE} for the WMAP first-year data. Note that we plot $[(\ell+1)/2\pi]c_\ell^{\text{TE}}$ and not $[l(\ell+1)/2\pi]c_\ell^{\text{TE}}$. This choice emphasizes the oscillatory nature of c_ℓ^{TE} . For clarity, the dotted line shows $c_\ell = 0$. The solid line shows the predicted signal based on the c_ℓ^{TT} power spectrum of temperature anisotropy; there are no free parameters. The TE correlation on degree angular scales ($\ell > 20$) is in excellent agreement with the signal expected from adiabatic CMB perturbations. The excess power at low ℓ indicates significant reionization at large angular scales.

angular scales ($\ell < 20$), the data show excess power compared to adiabatic models, suggesting significant reionization.

The *WMAP* detection of the acoustic structure in the TE spectrum confirms several basic elements of the standard paradigm. The amplitudes of the peak and antipeak are a measure of the thickness of the decoupling surface, while the shape confirms the assumption that the primordial fluctuations are adiabatic. Adiabatic fluctuations predict a temperature/polarization signal anticorrelated on large scales, with TE peaks and antipeaks located midway between the temperature peaks (Hu & Sugiyama 1994). The existence of TE correlations on degree angular scales also provides evidence for superhorizon temperature fluctuations at decoupling, as expected for inflationary models of cosmology (Peiris et al. 2003).

4. TEMPLATE POWER SPECTRA

Figure 7 demonstrates that the power spectrum of temperature-polarization correlations on degree angular scales can be predicted using the power spectrum of the temperature fluctuations alone. We use this for a third derivation of the TE cross-power spectrum, based on template matching in pixel space. For pixel sizes of a few degrees, the signal-to-noise ratio (S/N) for the temperature maps is much larger than 1 per multipole, while the S/N in the polarization maps is much less than 1. The likelihood function for the polarization measurement then has the simple form

$$\log L = \left(\mathbf{P} - \sum_{\ell} \alpha_{\ell} \mathbf{P}_{\text{pred}}^{\ell} \right)^T N^{-1} \left(\mathbf{P} - \sum_{\ell} \alpha_{\ell} \mathbf{P}_{\text{pred}}^{\ell} \right), \quad (12)$$

where \mathbf{P} is the measured polarization signal (a $2N_{\text{pixel}}$ vector), $\alpha_{\ell} = c_{\ell}^{\text{TE}}/c_{\ell}^{\text{TT}}$ is the polarization fraction at each ℓ , N is the pixel noise correlation matrix (a $2N_{\text{pixel}} \times 2N_{\text{pixel}}$ matrix), and

$$\begin{aligned} Q_{\text{pred}}^{\ell}(\mathbf{n}) &= \sum_m a_{\ell m} [{}_2 Y_{\ell m}(\mathbf{n}) + {}_{-2} Y_{\ell m}(\mathbf{n})], \\ U_{\text{pred}}^{\ell}(\mathbf{n}) &= i \sum_m a_{\ell m} [{}_2 Y_{\ell m}(\mathbf{n}) - {}_{-2} Y_{\ell m}(\mathbf{n})]. \end{aligned} \quad (13)$$

Here ${}_{\pm 2} Y_{\ell m}(\mathbf{n})$ are the spin harmonics, while $a_{\ell m}$ are the measured coefficients for an all-sky map of the CMB temperature. Imposing a cut to mask the Galactic plane introduces additional correlations; we avoid this by using the ‘‘internal’’ linear combination temperature map (Bennett et al. 2003c) without imposing a sky cut.

The maps Q_{pred} and U_{pred} represent the predicted polarization pattern based on the observed pattern of temperature anisotropy. We fit these template maps to the observed Q and U polarization maps to derive the polarization fraction α_{ℓ} and thus the c_{ℓ}^{TE} polarization cross-power spectrum. Minimizing the likelihood function yields the normal equations

$$K_{\ell\ell'} \alpha_{\ell'} = y_{\ell}, \quad (14)$$

where

$$y_{\ell} = \mathbf{P} N^{-1} \mathbf{P}_{\text{pred}}^{\ell}, \quad (15)$$

$$K_{\ell\ell'} = \mathbf{P}_{\text{pred}}^{\ell} N^{-1} \mathbf{P}_{\text{pred}}^{\ell'}. \quad (16)$$

These equations show the advantages of this approach. We compare the data with a template in pixel space, making it straightforward to include a spatially varying noise signal. We directly compare the measured polarization maps with a prediction based on the measured temperature maps, yielding a measurement of the TE cross-power spectrum in the observed sky unaffected by cosmic variance. We can thus more easily compute the errors on the measured polarization fraction. The input temperature map (Stokes I) is already corrected for foreground emission (much simpler in pixel space, where the unpolarized foregrounds are more easily measured), greatly reducing the foreground contribution to the cross-power spectra.

We thus compute the temperature-polarization cross-correlation using three disparate techniques: the two-point angular correlation function, a quadratic estimator for the power spectrum in Fourier space, and a template fit in pixel space. All methods are in good agreement despite their very dissimilar treatment of the data. All methods show a significant excess of power for $\ell < 10$.

5. REIONIZATION

WMAP detects statistically significant correlations between the CMB temperature and polarization. The signal on degree angular scales ($\ell > 20$) agrees with the signal expected in adiabatic models based solely on the temperature power spectrum, without any additional free parameters. We also detect power on large angular scales ($\ell < 10$) well in excess of the signal predicted by the temperature power spectrum alone. This signal cannot be explained by data processing, systematic errors, or foreground polarization and has a frequency spectrum consistent with a cosmological origin.

The signal on large angular scales has a natural interpretation as the signature of early reionization.¹¹ Both the temperature and temperature-polarization power spectra can be related to the power spectrum of the radiation field during scattering (Zaldarriaga 1997). Thomson scattering damps the temperature anisotropy and regenerates a polarized signal on scales comparable to the horizon. The existence of polarization on scales much larger than the acoustic horizon at decoupling implies significant scattering at more recent epochs.

5.1. Reionization in a Λ CDM Universe

If we assume that the Λ CDM model is the best description of the physics of the early universe, we can fit the observed temperature-polarization cross-power spectrum to derive the optical depth τ . We assume a step function for the ionization fraction x_e and use the CMBFAST code (Seljak & Zaldarriaga 1996) to predict the multipole moments as a function of optical depth. While this assumption is simplistic, our conclusions on optical depth are not very sensitive to details of the reionization history or the background cosmology.

Figure 8 compares the polarization cross-power spectrum c_{ℓ}^{TE} derived from the quadratic estimator with Λ CDM models with and without reionization. The rise in power for

¹¹ Although tensor modes can also generate TE correlations at large angular scales, tensor-to-scalar ratios r large enough to fit the *WMAP* TE data are ruled out by the *WMAP* TT data (Spergel et al. 2003).

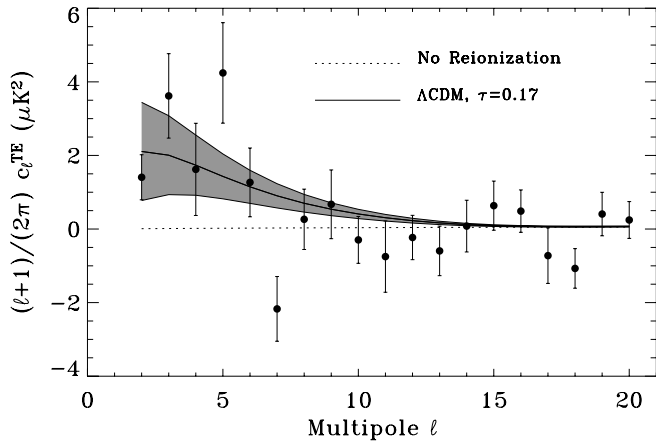


FIG. 8.—*WMAP* polarization cross-power spectra c_l^{TE} (filled circles) compared with Λ CDM models with and without reionization. The rise in power for $\ell < 10$ is consistent with reionization optical depth $\tau = 0.17 \pm 0.04$. The error bars on *WMAP* data reflect measurement errors only; adjacent points are slightly anticorrelated. The gray band shows the 68% confidence interval from cosmic variance. The value at $\ell = 7$ is particularly sensitive to the foreground correction.

$\ell < 10$ is clearly inconsistent with no reionization. We quantify this using a maximum likelihood analysis

$$L \propto \frac{\exp[-(1/2)\chi^2]}{|\mathbf{M}|^{1/2}}. \quad (17)$$

Figure 9 shows the relative likelihood $L/\max(L)$ for the optical depth τ assuming a Λ CDM cosmology, with all other parameters fixed at the values derived from the temperature power spectrum alone (Spergel et al. 2003). The likelihood for the five-band data corrected for foreground emission peaks at $\tau = 0.17 \pm 0.03$ (statistical error only): *WMAP* detects the signal from reionization at high statistical confidence.

A full error analysis for τ must account for systematic errors and foreground uncertainties. We propagate these effects by repeating the maximum likelihood analysis using different combinations of *WMAP* frequency bands and dif-

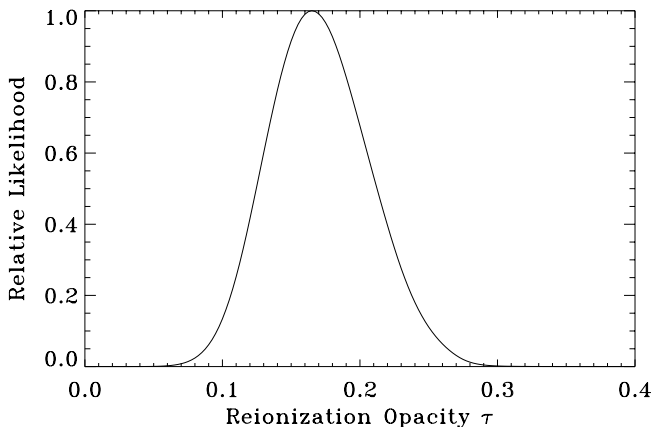


FIG. 9.—Likelihood function for optical depth τ for a Λ CDM cosmology, using all five *WMAP* frequency bands fitted to CMB plus foregrounds with foreground spectral index $\beta = -3.7$. After including systematic and foreground uncertainties, the optical depth is consistent with a value $\tau = 0.17$ with a 95% confidence range $0.09 \leq \tau \leq 0.28$.

ferent systematic error corrections. We correct $C^{IQ}(\theta)$ in each frequency band not for the best estimate of the systematic error templates but rather for the best estimate $\pm 1 \sigma$. We then fit the miscorrected $C^{IQ}(\theta, \nu)$ for a CMB piece plus a foreground piece (eq. [8]) and use the CMB piece in a maximum likelihood analysis for τ . The change in the best-fit value for τ as we vary the systematic error corrections propagates the uncertainties in these corrections. Systematic errors have a negligible effect on the fitted optical depth; altering the systematic error corrections changes the best-fit values of τ by less than 0.01.

The largest nonrandom uncertainty is the foreground separation. We assess the uncertainty in the foreground separation by repeating the entire systematic error analysis (using both standard and altered systematic error corrections) with the foreground spectral index $\beta = -3.7 \pm 0.8$ shifted 1σ up or down from the best-fit value. Table 2 shows the fitted optical depth τ and goodness-of-fit statistic χ^2 for different data combinations and foreground spectral indexes derived from the analysis of the two-point correlation function $C^{IQ}(\theta)$. The first set of rows shows values derived by simply co-adding the *WMAP* frequency channels, without any correction for foregrounds. Data at 41, 61, and 94 GHz (Q, V, and W bands), at which foregrounds are negligible, show similar values for τ ; the $\chi^2 \approx 66$ for 57 degrees of freedom indicates that the data are in agreement with reionized models. Adding additional low-frequency channels reduces the formal statistical uncertainty but introduces nonzero foreground contamination, as shown by the marked increase in χ^2 . The next three sets of rows show the results when the data are separated into CMB and foreground components (eq. [8]). All data combinations are now in agreement; we obtain nearly identical values for τ when fitting either the highest frequency data set QVW or the lowest frequency set KKaQ. The fitted optical depth is insensitive to the spectral index: varying the spectral index from -2.9 to -4.5 changes the fitted values by 0.02 or less. We adopt $\tau = 0.17 \pm 0.04$ as the best estimate for the optical depth to reionization, where the error bar reflects a 68% confidence level interval including statistical, systematic, and foreground uncertainties.

Spergel et al. (2003) include the TE data in a maximum likelihood analysis combining *WMAP* data with other astronomical measurements. The resulting value, $\tau = 0.17 \pm 0.06$, is consistent with the value derived from the TE data alone. The larger uncertainty reflects the effect of simultaneously fitting multiple parameters. The TE analysis propagates foreground uncertainties by reevaluating the likelihood using a different foreground spectral index. Since foreground affects only the lowest multipoles, the combined analysis propagates foreground uncertainty by doubling the statistical uncertainty in c_l^{TE} for $2 \leq \ell \leq 4$ to account for this effect.

5.2. Model-independent Estimate

An alternative approach avoids assuming any cosmological model and uses the measured temperature angular correlation function to determine the radiation power spectrum at recombination. This approach assumes that the best estimate of the three-dimensional radiation power spectrum is the *measured* angular power spectrum rather than a model fit to the angular power spectrum. Given the observed temperature power spectrum c_l^{TT} , we derive the predicted

TABLE 2
REIONIZATION OPTICAL DEPTH^a

Data Set	Method	β	τ^b	χ^2	$f(>WMAP)^c$
VW	Co-add	...	$0.14^{+0.05}_{-0.03}$	67.0	0.159
QVW	Co-add	...	0.15 ± 0.04	66.2	0.176
KaQVW	Co-add	...	0.14 ± 0.03	97.1	0.001
KKaQVW	Co-add	...	0.30 ± 0.02	359.8	0.0
KKaQ.....	Co-add	...	0.29 ± 0.01	476.6	0.0
QVW	Fit	-2.9	$0.12^{+0.19}_{-0.08}$	65.2	0.201
KaQVW	Fit	-2.9	$0.20^{+0.14}_{-0.05}$	69.8	0.101
KKaQVW	Fit	-2.9	0.22 ± 0.04	60.9	0.313
KKaQ.....	Fit	-2.9	0.20 ± 0.04	58.7	0.404
QVW	Fit	-3.7	$0.13^{+0.16}_{-0.07}$	66.1	0.180
KaQVW	Fit	-3.7	$0.19^{+0.13}_{-0.06}$	68.9	0.117
KKaQVW	Fit	-3.7	0.17 ± 0.03	55.4	0.491
KKaQ.....	Fit	-3.7	0.18 ± 0.04	48.0	0.772
QVW	Fit	-4.5	$0.13^{+0.15}_{-0.06}$	66.6	0.170
KaQVW	Fit	-4.5	$0.15^{+0.14}_{-0.05}$	68.2	0.140
KKaQVW	Fit	-4.5	0.16 ± 0.03	57.8	0.419
KKaQ.....	Fit	-4.5	0.16 ± 0.04	51.1	0.654

^a Optical depth τ fitted from $C^{\ell Q}(\theta)$ for various combinations of data and foreground corrections in a Λ CDM cosmology. There are 57 degrees of freedom for each fit.

^b Statistical uncertainties, quoted at 68% confidence.

^c Fraction of 1000 simulations of reionized Λ CDM models with χ^2 larger than the *WMAP* value.

polarization cross-power spectrum c_ℓ^{TE} (§ 4), which we then fit to the observed TE spectrum as a function of optical depth τ . We obtain $\tau = 0.16 \pm 0.04$, in excellent agreement with the value derived assuming a Λ CDM cosmology. We emphasize that the model-independent technique makes *no* assumptions about the cosmology. The fact that it agrees well with the best-fit model from the combined temperature and polarization data (Spergel et al. 2003) is an additional indication that the observed temperature-polarization correlations on large angular scales represent the imprint of physical conditions at reionization. The dependence on the underlying cosmology is small.

5.3. Early Star Formation

Reionization can also be expressed as a redshift z_r assuming an ionization history. We consider two simple cases. For instantaneous reionization with ionization fraction $x_e = 1$ at $z < z_r$, the measured optical depth corresponds to redshift $z_r = 17 \pm 3$. This conflicts with measurements of the Gunn-Peterson absorption trough in the spectra of distant quasars, which show neutral hydrogen present at $z \approx 6$ (Becker et al. 2001; Djorgovski et al. 2001; Fan et al. 2002). Reionization clearly did not occur through a single rapid phase transition. However, since absorption spectra are sensitive to even small amounts of neutral hydrogen, models with partial ionization $x_e \lesssim 1$ can have enough neutral column density to produce the Gunn-Peterson trough while still providing free electrons to scatter CMB photons and produce large-scale polarization. Direct Gunn-Peterson observations only imply a neutral hydrogen fraction $\gtrsim 1\%$ (Fan et al. 2002). Accordingly, we modify the simplest model to add a second transition: a jump from $x_e = 0$ to 0.5 at redshift z_r , followed by a second transition from $x_e = 0.5$

to 1 at redshift $z = 7$. Fitting this model to the measured optical depth yields $z_r \approx 20$. In reality, reionization is more complicated than simple step transitions. Allowing for model uncertainty, the measured optical depth is consistent with reionization at redshift $11 < z_r < 30$, corresponding to times $100 \text{ Myr} < t_r < 400 \text{ Myr}$ after the big bang (95% confidence).

Extrapolations of the observed ionizing flux to higher redshift lead to a predicted CMB optical depth between 0.04 and 0.08 (Miralda-Escudé 2002), lower than our best-fit values. The measured optical depth thus implies additional sources of ionizing flux at high redshift. An early generation of very massive (Population III) stars could provide the required additional heating. Tegmark et al. (1997) estimate that 10^{-3} of all baryons should have been in collapsed objects by $z = 30$. If these baryons formed massive stars, they would reionize the universe. However, photons below the hydrogen ionization threshold would destroy molecular hydrogen (the principal vehicle for cooling in early stars), driving the effective mass threshold for star formation to $\sim 10^8 M_\odot$ and impeding subsequent star formation (Haiman, Rees, & Loeb 1997; Gnedin & Ostriker 1997; Tegmark et al. 1997). X-ray heating and ionization (Venkatesan, Giroux, & Shull 2001; Oh 2001) may provide a loophole to this argument by enhancing the formation of H_2 molecules (Haiman, Abel, & Rees 2000).

Cen (2003) provides a physically motivated model of “double reionization” that resembles the two-step model above. A first generation of massive Population III stars initially ionizes the intergalactic medium. The increased metallicity of the intergalactic medium then produces a transition to smaller Population II stars, after which the reduced ionizing flux allows regeneration of a neutral hydrogen fraction. The ionization fraction remains at $x_e \approx 0.6$ until the global

star formation rate surpasses the recombination rate at $z = 6$, restoring $x_e = 1$. The predicted value $\tau = 0.10 \pm 0.03$ should be increased somewhat to reflect the higher *WMAP* values for the baryon density Ω_b and normalization σ_8 (Spergel et al. 2003). The contribution from ionized helium will also serve to increase τ (Venkatesan, Tumlinson, & Shull 2003; Wyithe & Loeb 2003). The *WMAP* determination of the optical depth indicates that ionization history must be more complicated than a simple instantaneous step function. While physically plausible models can reproduce the observed optical depth, reionization remains a complex process and cannot be fully characterized by a single number. A more complete determination of the ionization history requires evaluation of the detailed TE and EE power spectra (Kaplinghat et al. 2003; Hu & Holder 2003).

6. CONCLUSIONS

WMAP detects statistically significant correlations between the temperature and polarization maps. The correlations are inconsistent with instrument noise and are significantly larger than the upper limits established for potential systematic errors. The correlations are present in all *WMAP* frequency bands with similar amplitude from 23 to 94 GHz; fitting the data to a single power law in frequency yields a spectral index $\beta = -0.4 \pm 0.4$, consistent with a CMB signal ($\beta = 0$) and inconsistent with the measured spectral indexes for Galactic foreground emission. A two-component fit to a superposition of CMB and Galactic foregrounds yields a positive foreground detection in both curl and curl-free modes, with a best-fit spectral index $\beta = -3.7 \pm 0.8$, consistent with synchrotron emission of amplitude $0.5 \pm 0.1 \mu\text{K}^2$ antenna temperature at 41 GHz.

The fitted CMB component is robust against different data combinations and fitting techniques. On small angular scales ($\theta < 5^\circ$), the *WMAP* data show the temperature-polarization correlation expected from adiabatic perturbations in the temperature power spectrum. The data for

$\ell > 20$ agree well with the signal predicted solely from the temperature power spectra, with no additional free parameters.

The data show excess power on large angular scales ($\theta > 10^\circ$) compared to the predictions based on the temperature power spectrum alone. The excess power is well described by early reionization at redshift $z_r = 20_{-9}^{+10}$, corresponding to times $t_r = 180_{-80}^{+220}$ Myr after the big bang (95% confidence). A model-independent fit to reionization optical depth yields results consistent with the ΛCDM model. Our best estimate for the optical depth is $\tau = 0.17 \pm 0.04$ (68% confidence), where the error terms include statistical, systematic, and foreground uncertainties. This value is larger than expected given the detection of a Gunn-Peterson trough in the absorption spectra of distant quasars and implies that the universe has a complex ionization history.

The *WMAP* detection of early reionization opens a new frontier to explore the universe at redshift $6 < z < 30$. *WMAP*'s sensitivity to reionization is currently limited by instrument noise, both as direct statistical uncertainty and in the ability to better model and remove faint polarized foregrounds. Instrumental effects do not limit analysis of temperature-polarization correlations.¹² We are currently performing a more complete set of systematic error analyses in the individual Q and U maps. A future data release will include full-sky polarization maps and polarization power spectra.

The *WMAP* mission is made possible by the support of the Office of Space Sciences at NASA Headquarters and by the hard and capable work of scores of scientists, engineers, technicians, machinists, data analysts, budget analysts, managers, administrative staff, and reviewers.

¹²The TE power spectrum and covariance matrix are available at <http://lambda.gsfc.nasa.gov>.

APPENDIX A

QUADRATIC ESTIMATOR FOR TEMPERATURE-POLARIZATION POWER SPECTRUM

We estimate the temperature-polarization power spectrum from pixelized sky maps using the following formalism: We begin by expanding the temperature and polarization fluctuations in generalized spherical harmonics:

$$T(\mathbf{n}) = \sum_{\ell m} a_{\ell m} Y_{\ell m}(\mathbf{n}), \quad (\text{A1})$$

$$Q(\mathbf{n}) \pm iU(\mathbf{n}) = \sum_{\ell m} a_{\mp 2, \ell m \mp 2} Y_{\ell m}(\mathbf{n}). \quad (\text{A2})$$

We then decompose the polarization fluctuations into E - and B -like pieces:

$$a_{\pm 2, \ell m} = E_{\ell m} \pm iB_{\ell m}. \quad (\text{A3})$$

We can use the basic properties of the spherical harmonics,

$${}_N Y_{\ell m} = (-1)^N {}_{-N} Y_{\ell, -m}^*, \quad (\text{A4})$$

$$\int d\mathbf{n} {}_N Y_{\ell m}(\mathbf{n}) {}_N Y_{\ell' m'}^*(\mathbf{n}) = \delta_{\ell \ell'} \delta_{m m'}, \quad (\text{A5})$$

to derive

$$\begin{aligned} E_{\ell m} &= \frac{1}{2} \int d\mathbf{n} \{ Q(\mathbf{n}) [{}_2 Y_{\ell m}^*(\mathbf{n}) + {}_{-2} Y_{\ell m}^*(\mathbf{n})] \} - i \{ U(\mathbf{n}) [{}_2 Y_{\ell m}^*(\mathbf{n}) - {}_{-2} Y_{\ell m}^*(\mathbf{n})] \} , \\ B_{\ell m} &= -\frac{1}{2} \int d\mathbf{n} \{ U(\mathbf{n}) [{}_2 Y_{\ell m}^*(\mathbf{n}) + {}_{-2} Y_{\ell m}^*(\mathbf{n})] \} + i \{ Q(\mathbf{n}) [{}_2 Y_{\ell m}^*(\mathbf{n}) - {}_{-2} Y_{\ell m}^*(\mathbf{n})] \} . \end{aligned} \quad (\text{A6})$$

We can now generalize the approach of Hivon et al. (2002) to estimate the coupling terms. We multiply the temperature and polarization maps by a weighting function:

$$\tilde{T}_{\ell m} = \int d\mathbf{n} w^T(\mathbf{n}) T(\mathbf{n}) Y_{\ell m}^*(\mathbf{n}) , \quad (\text{A7})$$

$$\tilde{E}_{\ell m} = \frac{1}{2} \int d\mathbf{n} w^P(\mathbf{n}) \{ Q(\mathbf{n}) [{}_2 Y_{\ell m}^*(\mathbf{n}) + {}_{-2} Y_{\ell m}^*(\mathbf{n})] - i U(\mathbf{n}) [{}_2 Y_{\ell m}^*(\mathbf{n}) - {}_{-2} Y_{\ell m}^*(\mathbf{n})] \} , \quad (\text{A8})$$

$$\tilde{B}_{\ell m} = -\frac{1}{2} \int d\mathbf{n} w^P(\mathbf{n}) \{ U(\mathbf{n}) [{}_2 Y_{\ell m}^*(\mathbf{n}) + {}_{-2} Y_{\ell m}^*(\mathbf{n})] + i Q(\mathbf{n}) [{}_2 Y_{\ell m}^*(\mathbf{n}) - {}_{-2} Y_{\ell m}^*(\mathbf{n})] \} . \quad (\text{A9})$$

We expand the weighting function in spherical harmonics,

$$w(\mathbf{n}) = \sum_{\ell m} w_{\ell m} Y_{\ell m}(\mathbf{n}) , \quad (\text{A10})$$

and combine with equations (A1)–(A3) to yield

$$\begin{aligned} \tilde{T}_{\ell m} &= \sum_{\ell' m' \ell'' m''} w_{\ell' m'}^T T_{\ell'' m''} \int d\mathbf{n} Y_{\ell' m'}(\mathbf{n}) Y_{\ell'' m''}(\mathbf{n}) Y_{\ell m}^*(\mathbf{n}) , \\ \tilde{E}_{\ell m} &= \frac{1}{2} \sum_{\ell' m' \ell'' m''} w_{\ell' m'}^P \left\{ E_{\ell' m'} \int d\mathbf{n} Y_{\ell' m'}(\mathbf{n}) [{}_2 Y_{\ell' m'}(\mathbf{n}) {}_2 Y_{\ell m}^*(\mathbf{n}) + {}_{-2} Y_{\ell' m'}(\mathbf{n}) {}_{-2} Y_{\ell m}^*(\mathbf{n})] \right. \\ &\quad \left. + i B_{\ell m} \int d\mathbf{n} Y_{\ell' m'}(\mathbf{n}) [{}_2 Y_{\ell' m'}(\mathbf{n}) {}_2 Y_{\ell m}^*(\mathbf{n}) - {}_{-2} Y_{\ell' m'}(\mathbf{n}) {}_{-2} Y_{\ell m}^*(\mathbf{n})] \right\} , \\ \tilde{B}_{\ell m} &= \frac{1}{2} \sum_{\ell' m' \ell'' m''} w_{\ell' m'}^P \left\{ B_{\ell' m'} \int d\mathbf{n} Y_{\ell' m'}(\mathbf{n}) [{}_2 Y_{\ell' m'}(\mathbf{n}) {}_2 Y_{\ell m}^*(\mathbf{n}) + {}_{-2} Y_{\ell' m'}(\mathbf{n}) {}_{-2} Y_{\ell m}^*(\mathbf{n})] \right. \\ &\quad \left. - i E_{\ell m} \int d\mathbf{n} Y_{\ell' m'}(\mathbf{n}) [{}_2 Y_{\ell' m'}(\mathbf{n}) {}_2 Y_{\ell m}^*(\mathbf{n}) - {}_{-2} Y_{\ell' m'}(\mathbf{n}) {}_{-2} Y_{\ell m}^*(\mathbf{n})] \right\} . \end{aligned} \quad (\text{A11})$$

We can then use

$$\int d\mathbf{n} Y_{\ell m}^*(\mathbf{n}) Y_{\ell' m'}(\mathbf{n}) Y_{\ell'' m''}(\mathbf{n}) = (-1)^{N+m} \left[\frac{(2\ell+1)(2\ell'+1)(2\ell''+1)}{4\pi} \right]^{1/2} \begin{pmatrix} \ell & \ell' & \ell'' \\ -N & N' & N'' \end{pmatrix} \begin{pmatrix} \ell & \ell' & \ell'' \\ -m & m' & m'' \end{pmatrix} \quad (\text{A12})$$

to compute

$$\begin{pmatrix} \tilde{c}_{\ell}^{\text{TT}} \\ \tilde{c}_{\ell}^{\text{TE}} \\ \tilde{c}_{\ell}^{\text{TB}} \\ \tilde{c}_{\ell}^{\text{EE}} \\ \tilde{c}_{\ell}^{\text{BB}} \end{pmatrix} = \begin{pmatrix} \\ \\ M_{\ell\ell'}^{ab} \\ \\ \end{pmatrix} \begin{pmatrix} c_{\ell'}^{\text{TT}} \\ c_{\ell'}^{\text{TE}} \\ c_{\ell'}^{\text{TB}} \\ c_{\ell'}^{\text{EE}} \\ c_{\ell'}^{\text{BB}} \end{pmatrix} . \quad (\text{A13})$$

These expressions can be reduced using the symmetry and orthogonality properties of 3- j symbols, as given in equations (1.8) and (1.14) of Rotenberg et al. (1959). In particular, imaginary terms drop out, and summations over products of 3- j symbols with $-m$, m' , and m'' in the bottom row evaluate to $1/(2\ell''+1)$. After some algebra, the coupling terms reduce to

$$M_{\ell\ell'}^{\text{TT,TT}} = \frac{(2\ell'+1)}{4\pi} \sum_{\ell''} \mathcal{W}_{\ell''}^{\text{TT}} \begin{pmatrix} \ell & \ell' & \ell'' \\ 0 & 0 & 0 \end{pmatrix}^2 , \quad (\text{A14})$$

$$M_{\ell\ell'}^{\text{TE,TE}} = M_{\ell\ell'}^{\text{TB,TB}} = \frac{(2\ell'+1)}{8\pi} \sum_{\ell''} \mathcal{W}_{\ell''}^{\text{TP}} \begin{pmatrix} \ell & \ell' & \ell'' \\ 0 & 0 & 0 \end{pmatrix} \left[\begin{pmatrix} \ell & \ell' & \ell'' \\ -2 & 2 & 0 \end{pmatrix} + \begin{pmatrix} \ell & \ell' & \ell'' \\ 2 & -2 & 0 \end{pmatrix} \right] , \quad (\text{A15})$$

$$M_{\ell\ell'}^{EE,EE} = M_{\ell\ell'}^{BB,BB} = \frac{(2\ell' + 1)}{16\pi} \sum_{\ell''} \mathcal{W}_{\ell''}^{PP} \left[\begin{pmatrix} \ell & \ell' & \ell'' \\ -2 & 2 & 0 \end{pmatrix} + \begin{pmatrix} \ell & \ell' & \ell'' \\ 2 & -2 & 0 \end{pmatrix} \right] \left[\begin{pmatrix} \ell & \ell' & \ell'' \\ -2 & 2 & 0 \end{pmatrix} + \begin{pmatrix} \ell & \ell' & \ell'' \\ 2 & -2 & 0 \end{pmatrix} \right], \quad (\text{A16})$$

$$M_{\ell\ell'}^{EE,BB} = M_{\ell\ell'}^{BB,EE} = \frac{(2\ell' + 1)}{16\pi} \sum_{\ell''} \mathcal{W}_{\ell''}^{PP} \left[\begin{pmatrix} \ell & \ell' & \ell'' \\ -2 & 2 & 0 \end{pmatrix} - \begin{pmatrix} \ell & \ell' & \ell'' \\ 2 & -2 & 0 \end{pmatrix} \right] \left[\begin{pmatrix} \ell & \ell' & \ell'' \\ -2 & 2 & 0 \end{pmatrix} - \begin{pmatrix} \ell & \ell' & \ell'' \\ 2 & -2 & 0 \end{pmatrix} \right], \quad (\text{A17})$$

where

$$\mathcal{W}_{\ell}^{ab} = \sum_m w_{\ell m}^a w_{\ell m}^{b*}, \quad (\text{A18})$$

with a and b referring to either T or P. All of the other coupling terms are zero. Note that if we use different weighting functions for I , Q , and U , we increase the coupling between E - and B -modes.

APPENDIX B

UNIFORM TEMPERATURE WEIGHTING

If we use the full sky to compute the temperature spherical harmonic terms, then the cross-correlation term and its error matrix become particularly simple. For this case, $w_{00}^T = 1/(4\pi)^{1/2}$, and all other coupling terms are 0. In this limit, the measured c_{ℓ}^{TE} is just a constant times the true c_{ℓ}^{TE} ,

$$c_{\ell}^{\text{TE}} = \frac{\tilde{c}_{\ell}^{\text{TE}}}{f}, \quad (\text{B1})$$

where

$$f = \int w_E(\mathbf{n}) \frac{d\mathbf{n}}{4\pi}. \quad (\text{B2})$$

The covariance matrix for these terms is diagonal:

$$M_{\ell\ell} = \frac{c_{\ell}^{\text{TT}} \tilde{c}_{\ell}^{\text{EE}}}{(2\ell + 1)f^2}. \quad (\text{B3})$$

REFERENCES

- Baccigalupi, C., Burigana, C., Perrotta, F., De Zotti, G., La Porta, L., Maino, D., Maris, M., & Paladini, R. 2001, *A&A*, 372, 8
 Barnes, C., et al. 2003, *ApJS*, 148, 51
 Becker, R. H., et al. 2001, *AJ*, 122, 2850
 Bennett, C. L., et al. 1996, *ApJ*, 464, L1
 ———. 2003a, *ApJ*, 583, 1
 ———. 2003b, *ApJS*, 148, 1
 ———. 2003c, *ApJS*, 148, 97
 Bond, J. R., & Efstathiou, G. 1984, *ApJ*, 285, L45
 Brouw, W. N., & Spoelstra, T. A. T. 1976, *A&AS*, 26, 129
 Bruscoli, M., Tucci, M., Natale, V., Carretti, E., Fabbri, R., Sbarra, C., & Cortiglioni, S. 2002, *NewA*, 7, 171
 Cen, R. 2003, *ApJ*, 591, 12
 Coulson, D., Crittenden, R. G., & Turok, N. G. 1994, *Phys. Rev. Lett.*, 73, 2390
 Djorgovski, S. G., Castro, S., Stern, D., & Mahabal, A. A. 2001, *ApJ*, 560, L5
 Fan, X., et al. 2002, *AJ*, 123, 1247
 Gnedin, N. Y., & Ostriker, J. P. 1997, *ApJ*, 486, 581
 Haiman, Z., Abel, T., & Rees, M. J. 2000, *ApJ*, 534, 11
 Haiman, Z., Rees, M. J., & Loeb, A. 1997, *ApJ*, 484, 985
 Hinshaw, G. F., et al. 2003a, *ApJS*, 148, 63
 ———. 2003b, *ApJS*, 148, 135
 Hivon, E., Górski, K. M., Netterfield, C. B., Crill, B. P., Prunet, S., & Hansen, F. 2002, *ApJ*, 567, 2
 Hu, W., & Dodelson, S. 2002, *ARA&A*, 40, 171
 Hu, W., & Holder, G. P. 2003, *Phys. Rev. D*, submitted (astro-ph/0303400)
 Hu, W., & Sugiyama, N. 1994, *ApJ*, 436, 456
 Hu, W., & White, M. 1997, *Phys. Rev. D*, 56, 596
 Jarosik, N., et al. 2003, *ApJS*, 145, 413
 Kaiser, N. 1983, *MNRAS*, 202, 1169
 Kamionkowski, M., Kosowsky, A., & Stebbins, A. 1997, *Phys. Rev. D*, 55, 7368
 Kaplinghat, M., Chu, M., Haiman, Z., Holder, G. P., Knox, L., & Skordis, C. 2003, *ApJ*, 583, 24
 Kosowsky, A. 1996, *Ann. Phys.*, 246, 49
 Kovac, J., et al. 2002, *Nature*, 420, 772
 Lubin, P. M., & Smoot, G. F. 1981, *ApJ*, 245, 1
 Miralda-Escudé, J. 2002, *ApJ*, submitted (astro-ph/0211071)
 Oh, S. P. 2001, *ApJ*, 553, 499
 Page, L., et al. 2003a, *ApJ*, 585, 566
 ———. 2003b, *ApJS*, 148, 39
 Peiris, H., et al. 2003, *ApJS*, 148, 213
 Rees, M. J. 1968, *ApJ*, 153, L1
 Rotenberg, M., Bivins, R., Metropolis, N., & Wooten, J. K., Jr. 1959, *The 3-j and 6-j Symbols* (Cambridge: MIT)
 Seljak, U., & Zaldarriaga, M. 1996, *ApJ*, 469, 437
 Spergel, D. N., et al. 2003, *ApJS*, 148, 175
 Tegmark, M., et al. 1997, *ApJ*, 474, 1
 Tucci, M., Carretti, E., Cecchini, S., Nicastro, L., Fabbri, R., Gaensler, B. M., Dickey, J. M., & McClure-Griffiths, N. M. 2002, *ApJ*, 579, 607
 Uyaniker, B., Fuerst, E., Reich, W., Reich, P., & Wielebinski, R. 1998, *A&AS*, 132, 401
 ———. 1999, *A&AS*, 138, 31
 Venkatesan, A., Giroux, M. L., & Shull, J. M. 2001, *ApJ*, 563, 1
 Venkatesan, A., Tumlinson, J., & Shull, J. M. 2003, *ApJ*, 584, 621
 Wyithe, J. S. B., & Loeb, A. 2003, *ApJ*, 586, 693
 Zaldarriaga, M. 1997, *Phys. Rev. D*, 55, 1822
 Zaldarriaga, M., & Seljak, U. 1997, *Phys. Rev. D*, 55, 1830